

Dynamically generated edge states in topological Kondo insulators

Jan Werner^{1,*} and Fakher F. Assaad¹

¹*Institut für Theoretische Physik und Astrophysik,
Universität Würzburg, Am Hubland, D-97074 Würzburg, Germany*
(Dated: September 29, 2018)

Kondo insulators combine strong electronic correlations with spin orbit coupling and thereby provide a potential realization of correlated topological insulators. We present model calculations which allow us to study the onset of bulk coherence and concomitant topological edge states from the mixed valence to local moment regimes. Our real-space dynamical mean-field results include the detailed temperature dependence of the single particle spectral function on slab geometries as well as the temperature dependence of the topological invariant. The relevance of our calculations for candidate materials like SmB₆ is discussed.

PACS numbers: 71.27.+a, 71.10.Fd

The essence of heavy fermion systems is captured by the hybridization of narrow – nearly localized – and wide – delocalized – electronic bands^{1–3}. In the *high* temperature limit, the two systems essentially decouple, while at temperatures below the coherence scale a Fermi liquid emerges. The effective mass of the dressed quasiparticles, or inverse coherence temperature, can exceed by orders of magnitude the bare electronic mass. The Kondo insulating state occurs when there is precisely one localized and one delocalized electron per unit cell. It is the ultimate sign of coherence in the sense that the dynamically induced hybridized band structure is precisely half-filled, with the chemical potential right inside the hybridization gap. Based on mean-field theories which capture very well the ground state properties it has been argued^{4,5} that the Kondo insulating state can be a quantum spin Hall insulator^{6,7}, thus providing an explicit example of a correlation-induced topological state⁸: the topological Kondo insulating state (TKI).

The origin of the TKI can be traced back to the odd-parity wave-function of the nearly localized *f*-electrons hybridizing with even parity delocalized conduction electrons alongside strong spin-orbit coupling. Although the ground state of the TKI is adiabatically connected to the non-interacting quantum spin Hall state, correlation effects show up in a non-trivial temperature dependence of spectral functions. The TKI state provides an interpretation of the low temperature resistivity anomalies observed in many Kondo insulators⁹ such as SmB₆¹⁰, YbB₁₂^{11,12} or even Ce₃Bi₄Pt₃¹³. Recent ab-initio band structure calculations have classified SmB₆¹⁴ and YbB₁₂¹⁵ as topological insulator and respectively topological crystalline insulator. For SmB₆ it is experimentally^{16–19} concluded that the resistivity saturation originates from surface as opposed to bulk conductance. Additional evidence comes from the observation of a residual density of states at the Fermi level as the temperature $T \rightarrow 0$ ²⁰ as well as from photoemission studies^{21–23} which lead to the interpretation of a Fermi surface consisting of three pockets as appropriate for a topological insulator²⁴. The aim of this article is to provide a detailed numerical calculation of a minimal model

which captures generic features of the TKI state. We will scan from mixed valence to local moment regimes, map out the relevant energy scales, the topological invariant, and provide a temperature dependence analysis of the single particle spectral function on a slab geometry. In the next two sections we describe our model and methods. Details of the technical implementation can be found in the Appendix. Section III is devoted to a discussion of our results, both for bulk and boundary properties and in Sec. IV we conclude.

I. MODEL.

Following Ref.⁴ we will consider a Kramers doublet of almost localized *f*-electrons hybridizing with a delocalized conduction band. The corresponding Hamiltonian²⁵ is $\mathcal{H} = \mathcal{H}_0 + \mathcal{H}_U$ where

$$\mathcal{H}_0 = \sum_{k \in BZ} \begin{pmatrix} d_k^\dagger \\ f_k^\dagger \end{pmatrix}^T \begin{pmatrix} \mathbf{E}_d(k) & V^* \Phi^\dagger(k) \\ V \Phi(k) & \mathbf{E}_f(k) \end{pmatrix} \begin{pmatrix} d_k \\ f_k \end{pmatrix} \quad (1)$$

and $\mathcal{H}_U = U \sum_i n_{i\uparrow}^{(f)} n_{i\downarrow}^{(f)}$. The operator $d_k = (d_{k,\uparrow}, d_{k,\downarrow})$ creates a conduction electron with momentum k , while f_k creates an electron in the almost flat *f*-band. We consider a two-dimensional (2D) square lattice with $\mathbf{E}_d(k) = -2t_d(\cos(k_x) + \cos(k_y))\mathbf{1}$ and $\mathbf{E}_f(k) = (\varepsilon_f - 2t_f(\cos(k_x) + \cos(k_y)))\mathbf{1}$. The form factor $\Phi(\mathbf{k})$ encodes the spin-orbit coupling, which leads to the non-trivial band topology⁵. It reads $\Phi(k) = \vec{d}(k) \circ \vec{\sigma}$, where $\vec{d}(k) = (2 \sin(k_x), 2 \sin(k_y), 0)$ ²⁶. Although spin is not conserved, the Hamiltonian is block diagonal, so that due to time-reversal symmetry one can associate a conserved pseudo spin with the two Kramers conjugate blocks. \mathcal{H}_U describes a Hubbard interaction which acts only on the *f*-orbitals. Throughout this article we consider $V = 0.4t$, $\varepsilon_f = -6.0t$ and $t_d = t$ as well as a small hopping $t_f = -0.2t$ compatible with the almost localized character of the *f*-orbitals. The negative sign of t_f is necessary for the band inversion, which induces the topological

state²⁷. We vary the interaction strength to tune the system to both the mixed valence and local moment regimes. As appropriate for the Kondo insulating state, we consider the half-filled band case. In a previous study, we investigated the ground state bulk phase diagram²⁵, thus establishing the occurrence of distinct crystalline topological insulating states²⁸.

Here emphasis is placed on dynamical and topological finite temperature properties. We use periodic boundary conditions to infer bulk properties. In addition to that, we use a ribbon geometry of finite width N_y with open boundaries in the y-direction, but periodic boundary conditions in the x-direction, to directly investigate the dynamically induced topological surface states.

II. NUMERICAL METHODS

The method of choice to study paramagnetic phases of heavy fermion systems is the Dynamical Mean-Field Theory (DMFT)²⁹. The central approximation is the assumption of a local self-energy. This neglects non-local spacial correlations, while the frequency dependence is fully retained, and allows to capture the salient features of the paramagnetic heavy fermion state^{30–32}. By allowing for an inhomogeneous, site-dependent self-energy, we account for the inequivalence of sites in the open boundary case³³. Thus the lattice problem is mapped to a series of N_y impurity problems, which are coupled via the DMFT self-consistency condition

$$[\mathcal{G}(i\omega)]_{ii} = [G_{loc}(i\omega)]_{ii},$$

where \mathcal{G} and G_{loc} are the $(4N_y \times 4N_y)$ -dimensional impurity and local lattice Green's function, respectively. The numerically exact CT-HYB^{34,35} formulation of the quantum Monte Carlo algorithm, which becomes advantageous especially in the strong-coupling regime³⁶ is used to solve the resulting, auxiliary impurity problems. To obtain the self-energy from the impurity calculations, we employ an improved estimator based on higher-order correlation functions³⁷, which significantly reduces the statistical noise. We continue the converged result for the self-energy to the real-frequency axis^{38–40} by means of the stochastic analytical continuation method⁴¹, to obtain the orbital and momentum resolved spectral function.

$$A_i(k, \omega) = -\pi^{-1} \text{Im} [G(k, \omega^+)]_{ii} \quad (2)$$

$$G(k, \omega^+) = \left((G^{(0)}(k, \omega^+))^{-1} - \Sigma(\omega) \right)^{-1}$$

where $\omega^+ = \omega + i0^+$. Details of our approach can be found in Appendix A.

III. NUMERICAL RESULTS

In this section, we describe in some details our numerical results. The aim is to provide a systematic study of the evolution of relevant energy scales from the mixed valence to local moment regimes.

A. Topological invariant and coherence.

In TKI states the notion of coherence and the emergence of a topological band structure are intimately related. Following Ref.⁴² we have computed the topological invariant N_2 ⁴³ which in the framework of the DMFT takes the form:

$$N_2 = \text{Im} \left[\frac{d}{d\omega} K(\omega^+) \right]_{\omega=0} \text{ with } K(i\nu) = -\frac{1}{V\beta} \sum_{k, i\omega, \sigma} \quad (3)$$

$$\frac{\sigma}{2} \text{Tr} \left[\frac{\partial h_\sigma(k)}{\partial k_y} G_\sigma(k, i\omega + i\nu) \frac{\partial h_\sigma(k)}{\partial k_x} G_\sigma(k, i\omega) \right]$$

where σ is the pseudo spin. Instead of taking the derivative at real frequency $\omega = 0$, we approximate N_2 by the finite difference between the zeroth and first Matsubara frequencies. In the absence of interactions and at $T = 0$, N_2 corresponds to the quantized pseudo spin Hall conductivity in units of e^2/h . Since the TKI is adiabatically connected to a non-interacting state, the quantized nature of N_2 remains robust in the presence of interactions. In Fig. 1 we plot N_2 for various values of U/t as a function of temperature in units of T_N . The latter quantity is defined such that

$$N_2(T = T_N) = \frac{1}{2} \quad (4)$$

The value of T_N as a function of U/t is given in Fig. 2.

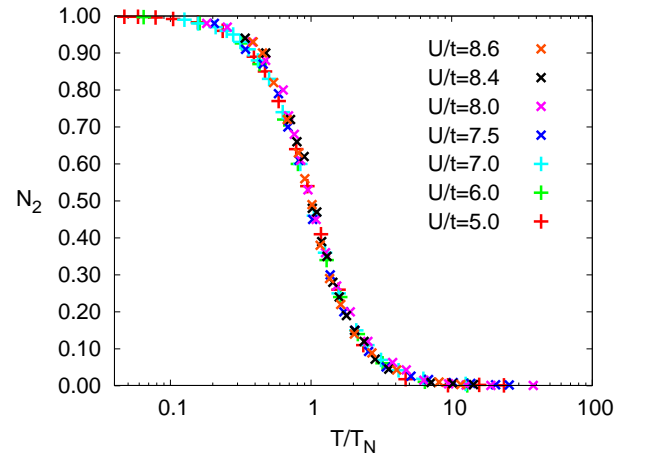


FIG. 1: Topological invariant N_2 over temperature in units of T_N , for different values of U/t .

As apparent, by plotting N_2 in units of T_N we achieve

a nice data collapse, thus suggesting that the formation of the topological band structure follows a single scale. That T_N is indeed nothing but the coherence scale T_{coh}

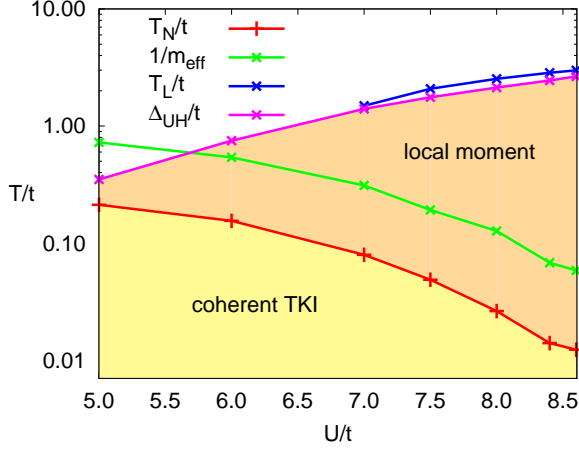


FIG. 2: Evolution of the different temperature scales with U .

can be seen by computing the bulk effective mass defined as

$$m_{eff} = 1 - \frac{d \Sigma_{bulk}(\omega)}{d\omega} \Big|_{\omega=0} \sim 1/T_{coh}.$$

The comparison of the energy scales in Fig. 2 reveals that T_N is proportional to the inverse of m_{eff} . A data collapse like the one in Fig. 1 suggests to relate T_N to the single impurity Kondo temperature T_K . However, for a lattice model like the PAM, in particular for mixed valence, T_K is not well-defined. Therefore we avoid the notion of the Kondo scale T_K . At least in the local-moment limit, namely in the Kondo lattice model, numerical studies find that at fixed particle number T_K and the coherence scale are closely related^{44,45}.

B. Local moment and mixed valence regimes.

In units of the hopping matrix element t and for the considered values of the Hubbard interaction the coherence scale varies roughly by an order of magnitude and interpolates between the mixed valence and local moment regimes. We can confirm this statement by considering the quantity

$$\Theta = 1 - \frac{\langle n_{\uparrow}^{(f)} n_{\downarrow}^{(f)} \rangle}{\langle n_{\uparrow}^{(f)} \rangle \langle n_{\downarrow}^{(f)} \rangle} \quad (5)$$

which is zero in the uncorrelated case, and approaches one for a local moment, since in this limit $\langle n_{\uparrow} n_{\downarrow} \rangle \rightarrow 0$. As can be seen in Fig. 3, Θ increases with lowering of the temperature, and saturates at the lowest temperatures.

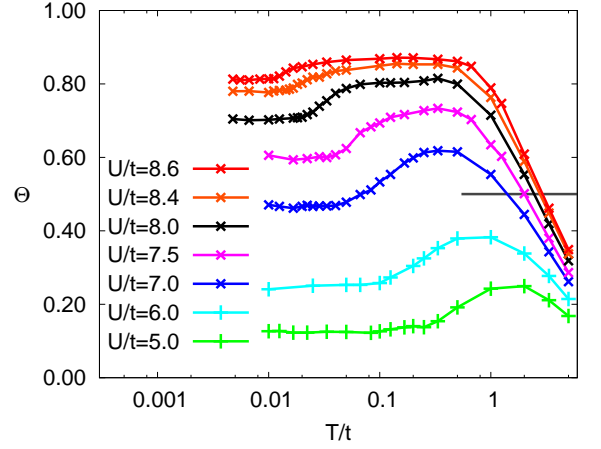


FIG. 3: Formation of the local moment as defined by Θ (see Eq. 5) at different values of U/t . The gray horizontal line indicates the threshold value for the local moment scale.

For sufficiently large U/t , there is a plateau beyond which Θ drops slightly. We attribute this drop to the enhanced itinerancy of the f -electrons – translating into a growth of the double occupancy – arising as coherence sets in. In fact, the energy scale at which Θ converges to its zero temperature value matches approximately the coherence scale. We define the temperature scale for the crossover to the local moment T_L by

$$\Theta(T = T_L) = 1/2. \quad (6)$$

This allows us to obtain values for T_L in the range $U/t \geq 7.0$. The so obtained local moment scale, T_L , is included in Fig. 2. It turns out that T_L can be well understood as the energy gap between the chemical potential and the upper Hubbard band $\Delta_{UH} = \varepsilon_f + U - \mu$, which is included for comparison. Because of this, we will use Δ_{UH} as a measure of the crossover scale to the local moment regime.

C. Temperature dependence of the spectral function.

Fig. 4 plots the temperature dependence of the total spectral function, $\sum_i A_i(k, \omega)$, on slab geometries in the local moment ($U/t = 8.4$) and mixed valence ($U/t = 5$) regimes. For both considered parameter sets, the bulk f -density of states is plotted in Figs. 5 and 6. In the local moment regime, the lower (upper) Hubbard bands are located well below (above) the Fermi energy. In contrast, in the mixed valence regime, the upper Hubbard band lies in the vicinity of the Fermi energy. The canonical particle-hole transformation, $d_k \rightarrow d_{k+Q}^\dagger$ and $f_k \rightarrow f_{k+Q}^\dagger$ where $Q = (\pi, \pi)$ maps the present results to the case where the lower Hubbard band lies in the vicinity of the chemical potential and the upper Hubbard band well above the

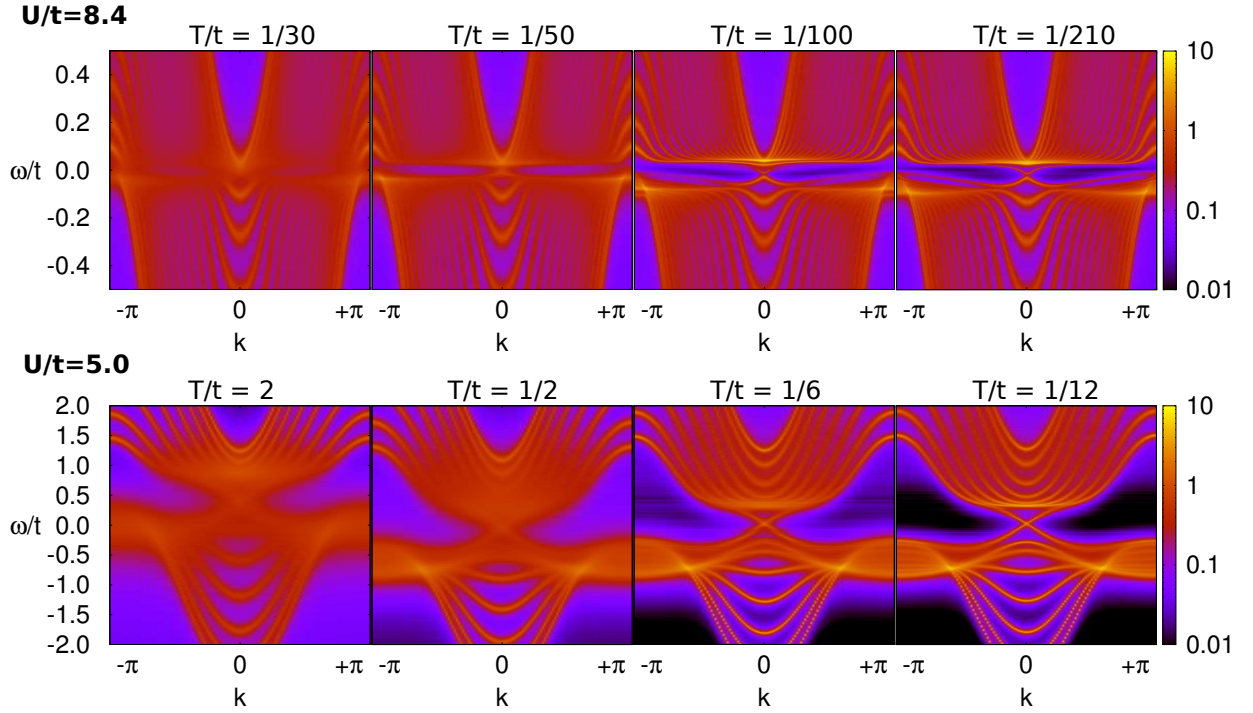


FIG. 4: Temperature dependence of the single particle spectral function in the local moment ($N_y = 16$, upper panel) and mixed valence regimes ($N_y = 8$, lower panel), projected to the one-dimensional surface Brillouin zone. Above the coherence temperature $T_N/t \approx 0.014$ at $U/t = 8.4$ and $T_N/t \approx 0.21$ at $U/t = 5$ one observes broad, incoherent, features out of which the bulk gap and helical surface state emerge as T drops below T_N .

Fermi energy. In both the mixed valence and local moment regimes, the coherence scale, T_N , marks the onset of the formation of the bulk band gap and the emergence of the helical edge state. In the mixed valence regime, there is a substantial reordering of spectral weight in the vicinity of the Fermi energy and at a temperature scale set by the coherence scale. In the local moment regime, coherence is accompanied by a *small* transfer of spectral weight from the upper and lower Hubbard bands to a region in the vicinity of the Fermi energy. This transfer of spectral weight reflects the enhanced itinerancy of the f -electrons below the coherence temperature. Above T_N incoherent features are detectable in the spectral function. In the local moment regime, this stems from spin flip scattering of conduction electrons off the well-formed local moments. In the mixed valence regime, incoherence should be assigned to Mott Hubbard physics⁴⁶. Below T_N one observes the Dirac cone with crossing point in the close vicinity of the Fermi energy. Hence, although the effective mass of the f -electrons varies by an order of magnitude, the effective mass of the edge state remains small. This observation is in accord with recent quantum oscillation experiments of Ref.¹⁹. Despite the very different pictures involved in the understanding of the mixed valence and local moment regimes, the temperature dependence of the low-lying features of the single particle spectral function show remarkable similarities when the

energy is measured in units of the coherence scale T_N . This is consistent with Fig. 1 which demonstrates that T_N is the only energy scale.

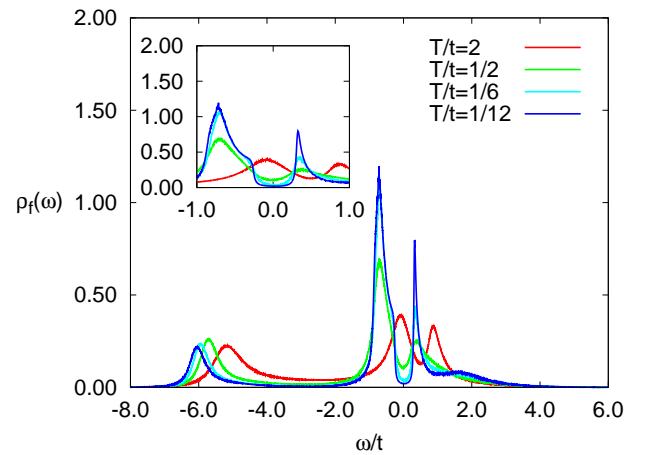


FIG. 5: Bulk density of states of the f -band as a function of temperature for $U/t = 5.0$.

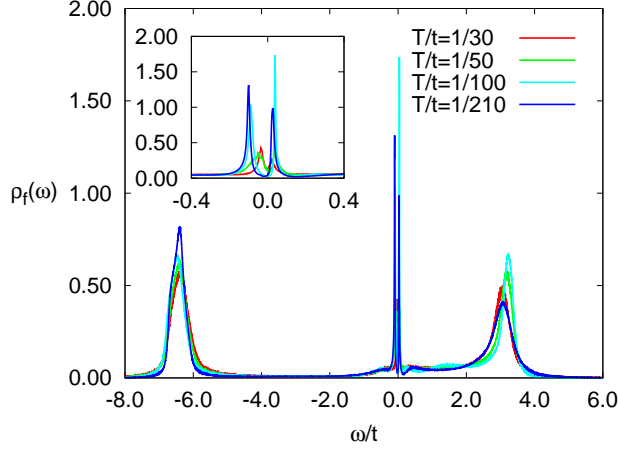


FIG. 6: Bulk density of states of the f -band as a function of temperature for $U/t = 8.4$.

IV. CONCLUSIONS

In summary, we have studied a model for topological Kondo insulators within real space DMFT+CTQMC. We have mapped out the relevant scales from the mixed valence to local moment regimes, and showed that the characteristic temperature scale below which the topological invariant N_2 saturates tracks the coherence temperature. Of particular importance for ARPES^{21–23} and quantum oscillation¹⁹ experiments is the single particle spectral function. We have computed this quantity on ribbon geometries so as to allow for the emergence of edge states. Throughout the considered parameter range, which covers an order of magnitude variation in the f -electron effective mass, we observe dynamically induced edge states below the bulk coherence temperature. To a first approximation the Fermi velocity of the edge state tracks the coherence temperature (inverse f -electron effective mass) but has a small effective mass since the Dirac cone crossing lies in the vicinity of the Fermi energy. This large difference between the surface and bulk f -electron effective masses is consistent with observations of Ref.¹⁹. Our model captures the minimal ingredients for the description of the TKI state. Many of the results – based only on topological considerations and the purely local Kondo effect – will carry over to more realistic situ-

ations found in possible candidate materials. Qualitative understanding of SmB_6 clearly requires to take a step beyond the Kramers doublet description of the f -state so as to take into account the cubic symmetry inherent to this material⁴⁷ as well as the chemical reconstruction of the SmB_6 surface⁴⁸.

Appendix A: Real-space DMFT

To study the system with open boundaries, we employ the real-space formulation of the Dynamical Mean Field Theory³³. In this approach, the inhomogeneous lattice system is mapped to a series of single impurity problems $j = 1 \dots N_y$, which can be described by the action

$$S_j = \int_0^\beta d\tau d\tau' \sum_\sigma f_\sigma^\dagger(\tau) \Delta_j(\tau - \tau') f_\sigma(\tau') + \int_0^\beta d\tau \mathcal{H}_{imp}(\tau). \quad (\text{A1})$$

The individual impurity problems differ in the hybridization function Δ_j , which is obtained by the self-consistency condition

$$\begin{aligned} \left(i\omega + \mu - \varepsilon_f - \Delta_j(i\omega) - \Sigma_j(i\omega) \right)^{-1} &= [\mathcal{G}(i\omega)]_{jj} \\ &= [G_{loc}(i\omega)]_{jj}. \end{aligned}$$

\mathcal{G} is the impurity Green's function, while the local lattice Green's function is given by

$$G_{loc}(i\omega) = \frac{1}{N_x} \sum_{k_x} \left((i\omega + \mu) \mathbf{1} - \mathbf{T}(k_x) - \Sigma(i\omega) \right)^{-1}.$$

It couples the different impurity problems and encodes the reduced coordination on the edge via \mathbf{T} , which is the Fourier-transform of the hopping and hybridization term plus on-site energy. It takes the form

$$\mathbf{T}(k_x) = \begin{pmatrix} H_{0,0} & H_{0,1} & 0 & \cdots \\ H_{1,0} & H_{1,1} & H_{1,2} & \cdots \\ 0 & H_{2,1} & H_{2,2} & \cdots \\ \vdots & \vdots & \vdots & \ddots \end{pmatrix}$$

where

$$H_{j,j} = \begin{pmatrix} -2t_d \cos(k_x) & 0 & 0 & 2V^* \sin(k_x) \\ 0 & -2t_d \cos(k_x) & 2V^* \sin(k_x) & 0 \\ 0 & 2V \sin(k_x) & \varepsilon_f - 2t_f \cos(k_x) & 0 \\ 2V \sin(k_x) & 0 & 0 & \varepsilon_f - 2t_f \cos(k_x) \end{pmatrix}, \quad H_{j+1,j} = H_{j,j+1}^\dagger = \begin{pmatrix} -t_d & 0 & 0 & iV \\ 0 & -t_d & -iV & 0 \\ 0 & iV & -t_f & 0 \\ -iV & 0 & 0 & -t_f \end{pmatrix}.$$

The self-energy is diagonal and obtained from the impurity calculations via the Dyson equation

$$\Sigma_{jk}(i\omega) = \delta_{jk} \Sigma_j(i\omega) = \delta_{jk} \left(\mathcal{G}_j^{(0)}(i\omega)^{-1} - (\mathcal{G}_j(i\omega))^{-1} \right).$$

To solve the impurity problems (A1), we employ the hybridization-expansion formulation of the continuous-

time QMC algorithm^{34,35}. This corresponds to an expansion of the partition function in powers of the hybridization around the local, atomic limit:

$$\begin{aligned} \frac{Z}{Z_{loc}} = & \sum_{k=0}^{+\infty} \sum_{\{\sigma, \sigma'\}} \frac{1}{k!} \int_0^\beta d\tau_1 \cdots d\tau_k \int_0^\beta d\tau'_1 \cdots d\tau'_k \times \quad (\text{A2}) \\ & \times \langle T_\tau f_{\sigma_1}^\dagger(\tau_1) f_{\sigma'_1}(\tau'_1) \cdots f_{\sigma_k}^\dagger(\tau_k) f_{\sigma'_k}(\tau'_k) \rangle_{loc} \times \\ & \times \frac{1}{k!} \det(\Delta(\tau_i - \tau'_j)). \end{aligned}$$

The expectation value of the time-ordered product of operators $\langle \dots \rangle_{loc}$ is taken with respect to the local impurity Hamiltonian \mathcal{H}_{imp} .

The integral of (A2) is evaluated by constructing a Markov chain of configurations C of operators $C = (f_{\sigma_1}^\dagger(\tau_1), f_{\sigma_1}(\tau'_1), \dots, f_{\sigma_k}^\dagger(\tau_k), f_{\sigma_k}(\tau'_k))$, which is updated by adding or removing pairs of creation and annihilation operators. To increase the acceptance rate, in particular at low temperatures, we introduce a third kind of update, namely a shift update. To be precise, we randomly pick a single operator from the whole sequence, which is then displaced along the imaginary time axis by a random shift $\Delta\tau$, i.e. $f_{\sigma_l}(\tau_l) \rightarrow f_{\sigma_l}(\tau_l + \Delta\tau)$.

The central quantity for the DMFT is the single-particle Green's function, or equivalently the self-energy. The conventional measurement of $\mathcal{G}(\tau)$ in the hybridization expansion CTQMC consists of accumulating

$$\mathcal{G}(\tau - \tau') = \sum_C \sum_{i,j=1}^k \delta(\tau - \tau_i) \delta(\tau' - \tau'_j) \delta_{\sigma_i \sigma_j} M_{ij}^{(C)}$$

where for a given configuration C , $M^{(C)}$ is the inverse of the matrix of hybridization functions: $(M^{(C)})_{ij}^{-1} = \Delta(\tau_i - \tau'_j)$. Finally, the self-energy is obtained via the Dyson equation. However, a more accurate estimate of the self-energy can be obtained by a different approach based on higher-order correlation function³⁷. In this method, and in the case of a local Hubbard interaction U , in addition to \mathcal{G} , one accumulates the correlation function

$$\Gamma(\tau - \tau') = \sum_C \sum_{i,j=1}^k \delta(\tau - \tau_i) \delta(\tau' - \tau'_j) \delta_{\sigma_i \sigma_j} n_{\bar{\sigma}_i}(\tau_i) M_{ij}$$

where $n_{\bar{\sigma}_i}(\tau_i)$ is the instantaneous occupation of the orbital with spin opposite to σ_i at time τ_i . For the local Hubbard U , the self-energy is related to this quantity and

the impurity Green's function by

$$\Sigma(i\omega) = U \Gamma(i\omega) \mathcal{G}^{-1}(i\omega).$$

An implementation of the hybridization expansion CTQMC solver, including the improved estimator for the self-energy, can be found in the ALPS package^{49,50}.

The analytical continuation of the results from Matsubara frequencies to real frequencies is done by the stochastic analytical continuation algorithm described in Ref. 51. The continuation to the real axis is done on the level of the self-energy, following Ref. 40. First, one subtracts the asymptotic value of the self-energy

$$\begin{aligned} \Sigma(i\omega) &= \Sigma_0 + \Sigma_1 \frac{1}{i\omega} + \dots \\ \Sigma'(i\omega) &= \frac{\Sigma(i\omega) - \Sigma_0}{\Sigma_1} \sim \frac{1}{i\omega} \end{aligned}$$

where

$$\Sigma_0 = \frac{U}{2} \langle n_f \rangle, \quad \Sigma_1 = \frac{U^2}{4} \langle n_f \rangle (2 - \langle n_f \rangle)$$

such that

$$\Sigma'(z) = -\frac{1}{\pi} \int d\omega \frac{\text{Im} \Sigma'(\omega^+)}{z - \omega}.$$

Analytical continuation provides $\text{Im}[\Sigma'(\omega^+)]$ from the knowledge of the Matsubara frequency QMC data, and from which one can readily compute $\Sigma(\omega^+)$ on the real frequency axis as well as the Green function: finally the momentum-resolved Green's function $\mathbf{G}(k_x, \omega^+)$ and orbital-resolved spectral function $A_j(k_x, \omega)$ on the real axis are obtained by

$$\begin{aligned} \mathbf{G}(k_x, \omega^+) &= \left((\omega^+ + \mu) \mathbf{1} - \mathbf{T}(k_x) - \mathbf{\Sigma}(\omega^+) \right)^{-1} \\ A_j(k_x, \omega) &= -\pi^{-1} \text{Im} [\mathbf{G}(k_x, \omega^+)]_{jj}. \end{aligned}$$

ACKNOWLEDGMENTS

We would like to thank C.-H. Min as well as F. Reinert for discussion. Funding from the DFG under the grant number AS120/6-2 (Forschergruppe FOR 1162) is acknowledged. We thank the Jülich Supercomputing Centre and the Leibniz-Rechenzentrum in Munich for generous allocation of CPU time.

* jwerner@physik.uni-wuerzburg.de

¹ Z. Fisk, H.R.Ott, T.M.Rice, and J. Smith, *Nature* **320**, 124 (1986).

² P. Coleman, in *Handbook of Magnetism and Advanced Magnetic Materials* (John Wiley & Sons, Ltd, Hoboken, NJ, 2007).

³ H. Tsunetsugu, M. Sigrist, and K. Ueda, *Rev. Mod. Phys.* **69**, 809 (1997).

⁴ M. Dzero, K. Sun, V. Galitski, and P. Coleman, *Phys. Rev. Lett.* **104**, 106408 (2010).

⁵ M. Dzero, K. Sun, P. Coleman, and V. Galitski, *Phys. Rev. B* **85**, 045130 (2012).

- ⁶ M. Z. Hasan and C. L. Kane, *Rev. Mod. Phys.* **82**, 3045 (2010).
- ⁷ X.-L. Qi and S.-C. Zhang, *Rev. Mod. Phys.* **83**, 1057 (2011).
- ⁸ M. Hohenadler and F. F. Assaad, *J. Phys.: Condens. Matter* **25**, 143201 (2013).
- ⁹ P. Riseborough, *Advances in Physics* **3**, 49 (2000).
- ¹⁰ J. W. Allen, B. Batlogg, and P. Wachter, *Phys. Rev. B* **20**, 4807 (1979).
- ¹¹ F. Iga, N. Shimizu, and T. Takabatake, *Journal of Magnetism and Magnetic Materials* **177/181**, Part 1, 337 (1998), international Conference on Magnetism.
- ¹² M. Batkov, I. Batko, E. Konovalova, N. Shitsevalova, and Y. Paderno, *Physica B: Condensed Matter* **378/380**, 618 (2006), proceedings of the International Conference on Strongly Correlated Electron Systems {SCES} 2005 Proceedings of the International Conference on Strongly Correlated Electron Systems.
- ¹³ M. F. Hundley, P. C. Canfield, J. D. Thompson, Z. Fisk, and J. M. Lawrence, *Phys. Rev. B* **42**, 6842 (1990).
- ¹⁴ F. Lu, J. Zhao, H. Weng, Z. Fang, and X. Dai, *Phys. Rev. Lett.* **110**, 096401 (2013).
- ¹⁵ H. Weng, J. Zhao, Z. Wang, Z. Fang, and X. Dai, *Phys. Rev. Lett.* **112**, 016403 (2014).
- ¹⁶ S. Wolgast, Ç. Kurdak, K. Sun, J. W. Allen, D.-J. Kim, and Z. Fisk, *Phys. Rev. B* **88**, 180405(R) (2013).
- ¹⁷ X. Zhang, N. P. Butch, P. Syers, S. Ziemak, R. L. Greene, and J. Paglione, *Phys. Rev. X* **3**, 011011 (2013).
- ¹⁸ D. J. Kim, S. Thomas, T. Grant, J. Botimer, Z. Fisk, and J. Xia, *Scientific Reports* **3**, 3150 (2013).
- ¹⁹ G. Li, Z. Xiang, F. Yu, T. Asaba, B. Lawson, P. Cai, C. Tinsman, A. Berkley, S. Wolgast, Y. S. Eo, D.-J. Kim, C. Kurdak, J. W. Allen, K. Sun, X. H. Chen, Y. Y. Wang, Z. Fisk, and L. Li, *arXiv:1306.5221*.
- ²⁰ M. M. Yee, Y. He, A. Soumyanarayanan, D.-J. Kim, Z. Fisk, and J. E. Hoffman, *arXiv:1308.1085* (2013).
- ²¹ E. Frantzeskakis, N. de Jong, B. Zwartsenberg, Y. K. Huang, Y. Pan, X. Zhang, J. X. Zhang, F. X. Zhang, L. H. Bao, O. Tegus, A. Varykhalov, A. de Visser, and M. S. Golden, *Phys. Rev. X* **3**, 041024 (2013).
- ²² M. Neupane, N. Alidoust, S.-Y. Xu, T. Kondo, Y. Ishida, D. J. Kim, C. Liu, I. Belopolski, Y. J. Jo, T.-R. Chang, H.-T. Jeng, T. Durakiewicz, L. Balicas, H. Lin, A. Bansil, S. Shin, Z. Fisk, and M. Z. Hasan, *Nat Commun* **4**, (2013).
- ²³ C.-H. Min, P. Lutz, S. Fiedler, B. Y. Kang, B. K. Cho, H.-D. Kim, H. Bentmann, and F. Reinert, *arXiv:1312.1834* (2013).
- ²⁴ L. Fu and C. L. Kane, *Phys. Rev. B* **76**, 045302 (2007).
- ²⁵ J. Werner and F. F. Assaad, *Phys. Rev. B* **88**, 035113 (2013).
- ²⁶ M.-T. Tran, T. Takimoto, and K.-S. Kim, *Phys. Rev. B* **85**, 125128 (2012).
- ²⁷ M. Legner, A. Rüegg, and M. Sigrist, *arXiv:1312.3639* (2013).
- ²⁸ R.-J. Slager, A. Mesaros, V. Juricic, and J. Zaanen, *Nat Phys* **9**, 98 (2013).
- ²⁹ A. Georges, G. Kotliar, W. Krauth, and M. J. Rozenberg, *Rev. Mod. Phys.* **68**, 13 (1996).
- ³⁰ T. Pruschke, R. Bulla, and M. Jarrell, *Phys. Rev. B* **61**, 12799 (2000).
- ³¹ K. S. D. Beach and F. F. Assaad, *Phys. Rev. B* **77**, 205123 (2008).
- ³² L. C. Martin, M. Bercx, and F. F. Assaad, *Phys. Rev. B* **82**, 245105 (2010).
- ³³ M. Potthoff and W. Nolting, *Euro. Phys. J. B* **8**, 555 (1999).
- ³⁴ P. Werner, A. Comanac, L. de Medici, M. Troyer, and A. J. Millis, *Phys. Rev. Lett.* **97**, 076405 (2006).
- ³⁵ P. Werner and A. J. Millis, *Phys. Rev. B* **74**, 155107 (2006).
- ³⁶ E. Gull, P. Werner, A. J. Millis, and M. Troyer, *Phys. Rev. B* **76**, 235123 (2007).
- ³⁷ H. Hafermann, K. R. Patton, and P. Werner, *Phys. Rev. B* **85**, 205106 (2012).
- ³⁸ X. Wang, E. Gull, L. de Medici, M. Capone, and A. J. Millis, *Phys. Rev. B* **80**, 045101 (2009).
- ³⁹ S. Fuchs, E. Gull, M. Troyer, M. Jarrell, and T. Pruschke, *Phys. Rev. B* **83**, 235113 (2011).
- ⁴⁰ F. Goth, D. J. Luitz, and F. F. Assaad, *Phys. Rev. B* **88**, 075110 (2013).
- ⁴¹ K. S. D. Beach, *arXiv:cond-mat/0403055* (2004).
- ⁴² T. Yoshida, S. Fujimoto, and N. Kawakami, *Phys. Rev. B* **85**, 125113 (2012).
- ⁴³ G. E. Volovik, *The Universe in a Helium Droplet* (Oxford University Press, Oxford, 2009).
- ⁴⁴ S. Burdin, A. Georges, and D. R. Grempel, *Phys. Rev. Lett.* **85**, 1048 (2000).
- ⁴⁵ F. F. Assaad, *Phys. Rev. B* **70**, 020402(R) (2004).
- ⁴⁶ M. Imada, A. Fujimori, and Y. Tokura, *Rev. Mod. Phys.* **70**, 1039 (1998).
- ⁴⁷ V. Alexandrov, M. Dzero, and P. Coleman, *Phys. Rev. Lett.* **111**, 226403 (2013).
- ⁴⁸ Z.-H. Zhu, A. Nicolaou, G. Levy, N. P. Butch, P. Syers, X. F. Wang, J. Paglione, G. A. Sawatzky, I. S. Elfimov, and A. Damascelli, *Phys. Rev. Lett.* **111**, 216402 (2013).
- ⁴⁹ B. Bauer, L. D. Carr, H. G. Evertz, A. Feiguin, J. Freire, S. Fuchs, L. Gamper, J. Gukelberger, E. Gull, S. Guertler, A. Hehn, R. Igarashi, S. V. Isakov, D. Koop, P. N. Ma, P. Mates, H. Matsuo, O. Parcollet, G. Pawowski, J. D. Picon, L. Pollet, E. Santos, V. W. Scarola, U. Schollwöck, C. Silva, B. Surer, S. Todo, S. Trebst, M. Troyer, M. L. Wall, P. Werner, and S. Wessel, *Journal of Statistical Mechanics: Theory and Experiment* **2011**, P05001 (2011), see also <http://alps.comp-phys.org>.
- ⁵⁰ E. Gull, P. Werner, S. Fuchs, B. Surer, T. Pruschke, and M. Troyer, *Computer Physics Communications* **182**, 1078 (2011).
- ⁵¹ K. S. D. Beach, *arXiv:0403055* (2004).